Photoacoustic Gas Detection: Optical Excitation Tailored to Acoustic Mode Structure of the Resonant Cell

Giovanni Gibertoni[1,2,*], Daniele Goldoni[1], Ada Fort[3], Enza Panzardi[3], Marco Mugnaini[3], and Luigi Rovati[1,5]

***Abstract*—This work presents a comparative study on how different optical-excitation geometries influence the photoacoustic (PA) response of a resonant gas sensor. Two excitation strategies are experimentally evaluated: a narrow-focused laser diode (LD) beam and a broader distributed light-emitting diode (LED) source at 405 nm using a ring-shaped resonant PA cell designed for NO_2 detection. By modifying the optical confinement and the spatial distribution of absorbed energy, the two sources excite the acoustic field in fundamentally different ways in terms of modal excitation, background generation, and gas-sensing performance. Results show that the spatial distribution of absorbed optical energy strongly affects the optical–acoustic coupling, with direct impact on sensitivity and baseline signal. Under comparable optical power levels, LED-based excitation yielded sensitivities on the order of 17–28 $\mathrm{mV\,ppm^{-1}}$, whereas LD excitation achieved sensitivities of 52.6 $\mathrm{mV\,ppm^{-1}}$ and up to 83.0 $\mathrm{mV\,ppm^{-1}}$ depending on the driving conditions. Moreover, the combination of a tightly focused LD excitation and output optical window allowing beam transmission through the cavity,significantly reduced the PA baseline signal level, preserving more than 90% of the available measurement system dynamic range. In contrast, the same geometrical approach provided only marginal baseline improvement for the focused LED source. These results confirm that proper control of the excitation geometry within resonant PA cells substantially improves optical-to-acoustic transduction efficiency and measurement stability, supporting the development of compact photoacoustic sensors suitable for high-sensitivity applications such as trace-gas detection and biomedical sensing.**

***Index Terms*—photoacoustic spectroscopy, resonant photoacoustic sensing, acoustic resonator, optical–acoustic coupling, gas sensing, LED excitation, laser diode.**

I. Introduction

Photoacoustic spectroscopy (PAS) is a well-established technique for trace gas detection, particularly attractive due to its capability to enable measurements over several orders of magnitude, which makes it suitable for applications in environmental monitoring and emerging biomedical fields [1]–[3]. It is based on the generation of acoustic waves following the periodic heating of an absorbing medium by a modulated light source [4]–[7]. The absorbed optical energy induces localized pressure fluctuations, which are detected by a microphone or other acoustic transducers and converted into an electrical signal whose amplitude is proportional to the gas concentration. When resonant operating modes are used, the modulation frequency of the optical source is matched to one of the acoustic resonator eigenfrequencies. Under this condition, the generated acoustic wave is amplified by a factor proportional to the cavity quality factor Q, which depends on the cell geometry, boundary losses, and gas properties [8], [9]. For this reason, resonant cells are typically designed to operate at a well-defined mode, enabling maximization of the acoustic signal at the corresponding pressure antinode, where the acoustic transducer must be properly positioned [10], [11]. The performance of a photoacoustic system is governed by three main factors: the efficiency of the optical-to-acoustic conversion, the acoustic amplification provided by the resonator, and the characteristics of the transducer and electronics [12], [13]. In the last decade, major advances in solid-state light sources, including high-power LEDs and laser diodes (LDs), have fostered the development of compact and low-cost photoacoustic instruments [14]–[16]. LED-based excitation provides excellent reliability, wide spectral coverage, and cost effectiveness, but typically suffers from lower radiant intensity and poor beam collimation compared with lasers [17], [18]. Conversely, laser-based PAS achieves higher energy density and easier optical focusing, resulting in improved signal-to-noise ratio (SNR) and detection limits in the sub-ppm or even ppb range [2], [19], [20]. Recent studies have demonstrated that by proper optimization of the excitation geometry, both LED and LD sources can yield high sensitivity suitable for trace detection [21]–[24].

The geometry of the resonant cavity plays a central role in determining the spatial overlap between the optical excitation field and the pressure distribution of the acoustic mode [12], [13]. Several cell designs have been proposed to improve confinement and uniformity of the acoustic field, including cylindrical [9], dumbbell-shaped [10], and microcavity configurations [11], [25]. Among these, we focus in this study on a ring-shaped resonant cell, previously introduced by Fort *et al.* in [21]. This structure has demonstrated enhanced performance in terms of spatial overlap between the optical excitation path and its fundamental acoustic mode, mainly due to its intrinsic symmetry. The resonator geometry was previously optimized through analytical modeling and finite-element method (FEM) simulations, as detailed in [21]. The optimization process was aimed at maximizing the acoustic response while ensuring a suitable quality factor and robustness against perturbations. The FEM analysis of this configuration shows that the fundamental mode, occurring approximately at 4 kHz for the optimized geometry, exhibits two diametrically opposed antinodes; this feature enables an optimal placement of both the optical source and the acoustic transducer, thereby maximizing the photoacoustic signal, whose amplitude scales

[1]Department of Engineering "Enzo Ferrari", University of Modena and Reggio Emilia, Modena, Italy.
[2]Department of Biomedical, Metabolic and Neural Sciences, University of Modena and Reggio Emilia, Modena, Italy.
[3]Department of Information Engineering and Mathematical Sciences, University of Siena, Siena, Italy.
[4]InterMech MO.RE. (Interdepartmental Centre for Advanced Mechanics and Mechatronics), University of Modena and Reggio Emilia, Modena, Italy.
*Corresponding author: Giovanni Gibertoni (email: giovanni.gibertoni@unimore.it).

with the coupling between the optical excitation and the acoustic field [4], [22].

Previous LED-based implementations of this PA cell [21] placed the optical source directly at the chamber entrance, producing a divergent illumination pattern and partial optical confinement. Residual reflections of the LED radiation within the cavity produced a measurable background signal even in the absence of absorbing gas, limiting the actual sensing performance of the sensing system [15], [25].

In the present work, we investigate how optical-source characteristics and excitation geometry affect the coupling to the fundamental acoustic mode, thus shaping the photoacoustic response of the sensing system. Starting from the setup proposed in [21], we analyze how different optical-excitation configurations determine the spatial distribution of absorbed energy and the resulting modal excitation; we also consider a single-pass geometry in which the excitation light is not confined within the resonator structure, thereby preventing residual light from interacting with the cavity boundaries. To experimentally validate the concept, we perform a comparative study between focused LED and LD excitation with a wavelength of 405 nm. This wavelength was selected as it lies within a strong absorption band of NO_2 in the near-UV region, as confirmed by both high-resolution spectroscopic data from the HITRAN2020 database [26] and by literature cross-section measurements [27]. NO_2 is used here as a representative test case; however, the proposed approach is general and can be extended to other gases and wavelengths. Both sources are characterized by optical power–current behavior, beam profile, and focusing efficiency. Gas measurements with controlled NO_2 concentrations (0–50 ppm) assess sensitivity, linearity, SNR, and baseline noise. The results show that LD excitation (narrow beam), due to its superior focusing, yields higher sensitivity and a more reliable PA response than the LED under comparable conditions. This is not a mere LED–LD comparison: the sources are used as a case study to elucidate the physical mechanisms governing optical–acoustic coupling and how the optical-field distribution affects PA-generation efficiency.While the gas sensing performance of the system has been thoroughly characterized in previous studies [21], [28], [17] the present work focuses instead on the role of optical–acoustic coupling and its impact on the generated PA signal. This perspective provides a deeper insight into the underlying physical mechanisms and offers useful guidelines for the design of optimized photoacoustic sensing systems.

II. Theoretical Framework for Optical–Acoustic Coupling in a Toroidal Resonator

The photoacoustic pressure wave generated in an absorbing gas follows the forced acoustic wave equation, where the absorbed optical power acts as a thermal source term. In its standard form, the pressure field satisfies the inhomogeneous wave equation [6] as:

$$\nabla^2 p(\mathbf{r},t) - \frac{1}{c^2}\frac{\partial^2 p(\mathbf{r},t)}{\partial t^2} = -\frac{(\gamma-1)}{c^2}\frac{\partial H(\mathbf{r},t)}{\partial t} \tag{1}$$

where $p(\mathbf{r},t)$ is the acoustic pressure at position $\mathbf{r}$, in time, c is the speed of sound, γ the ratio of specific heats, and $H(\mathbf{r},t)$ is the volumetric heating rate generated by optical absorption. Under sinusoidal modulation at angular frequency ω, the heating term takes the form:

$$H(\mathbf{r},t) = \alpha(\lambda) I(\mathbf{r}) e^{j\omega t} \tag{2}$$

where $\alpha(\lambda)$ is the absorption coefficient of gas at wavelength λ, and $I(\mathbf{r})$ the spatial intensity distribution of the optical source at position $\mathbf{r}$. The spatial profile of $I(\mathbf{r})$, therefore, directly determines how efficiently the absorbed optical energy is converted into acoustic pressure [29]. For a ring-shaped cavity, with major radius R and minor radius a, under the slender-torus approximation ($a << R$), the cross-sectional dimensions are much smaller than the azimuthal path length. In this case, it is convenient to describe the system using the azimuthal coordinate $\Phi \in [0, 2\pi)$ along the central circumference of the torus, with curvilinear coordinate $s = R\Phi$. As a result, radial and polar variations of the acoustic field can be neglected to first order, and acoustic propagation is predominantly distributed along the azimuthal direction [21], [30]. Under these assumptions, The position vector $\mathbf{r}$ can be restricted to the toroidal centerline and parameterized as $\mathbf{r}_{\text{torus}} = (R, \Phi, \theta = \pi/2)$ in toroidal coordinates (equivalently, $\mathbf{r}_{\text{torus}} = (R, \Phi, z = 0)$ in cylindrical coordinates). Under this assumption, the full three-dimensional pressure field $p(\mathbf{r},t)$ in Eq. 1 can be approximated by a one-dimensional forced Helmholtz equation. Therefore, under harmonic excitation, the pressure field can be written as [4]:

$$p(\mathbf{r}_{\text{torus}},t) = \left[\sum_{n=-\infty}^{+\infty} A_n(\omega)\, e^{jn\Phi}\right] e^{j\omega t}. \tag{3}$$

where the spatial dependence along the azimuthal coordinate is expanded in a complex Fourier series. Similarly, under the same approximation, the azimuthal distribution of absorbed optical power can be expressed as:

$$H(\mathbf{r}_{\text{torus}},t) = F(\Phi) e^{j\omega t} \tag{4}$$

where $F(\Phi) = \sum_{n=-\infty}^{+\infty} M_n e^{jn\Phi}$, and the modal coupling coefficients M_n, are defined as

$$M_n = \frac{1}{2\pi}\int_0^{2\pi} H(\Phi) e^{-jn\Phi} d\Phi. \tag{5}$$

By substituting the above expansions into the one-dimensional forced Helmholtz equation and exploiting the orthogonality of the exponential basis, the amplitude of the n-th azimuthal mode, including dissipative effects, is obtained as

$$A_n(\omega) = \frac{j\omega(\gamma-1)}{c^2}\frac{M_n}{(\frac{n}{R})^2 - k^2 + j\frac{k(n/R)}{Q_n^2}} \tag{6}$$

where $k = \omega/c$ and Q_n is the quality factor of the n-th mode, accounting for viscous, thermal, radiation, and wall-interaction losses [8], [9], [25]:

$$\frac{1}{Q_n} = \frac{1}{Q_{vis}} + \frac{1}{Q_{therm}} + \frac{1}{Q_{rad}} + \frac{1}{Q_{wall}}. \tag{7}$$

These results highlight the role of excitation geometry in determining the optical–acoustic coupling. It is worth noting that, in photoacoustic systems, background signals at the

excitation frequency may arise even in the absence of the target gas ($\alpha(\lambda) = 0$). These contributions are mainly associated with non-selective absorption processes, including residual absorption by carrier gases and parasitic heating of the cavity walls induced by the optical beam, which generate pressure fluctuations indistinguishable from the target photoacoustic signal and may limit the available dynamic range.

Building on this formulation, different optical excitation sources produce distinct spatial absorption patterns, leading to different modal coupling coefficients M_n. In the following, to highlight the role of excitation geometry, two limiting cases are considered. Here $H(\Phi)$ denotes the cross-section-averaged absorbed optical power distribution along the azimuthal coordinate, normalized such that the total absorbed optical power is:

$$P_\Phi = \int_0^{2\pi} H(\Phi) d\Phi. \tag{8}$$

i) Highly localized excitation (δ-like limit)
A tightly focused beam (e.g., a laser diode, LD) produces a highly localized illumination pattern along the azimuthal coordinate. In the limit of vanishing beam width, the absorbed power distribution can be approximated as a δ-like function centered at Φ_0:

$$H(\Phi) = P_\Phi \delta(\Phi - \Phi_0) \tag{9}$$

Substituting into Eq. 4, the modal coupling coefficients become:

$$M_n = \frac{P_\Phi}{2\pi} e^{-jn\Phi_0}, \tag{10}$$

This result shows that all azimuthal modes are excited with comparable magnitude, independently of the mode order n, while the phase depends on the beam position. Therefore, a highly localized excitation produces a broad modal spectrum, efficiently driving both fundamental and higher-order modes. While this may enhance the peak response at resonance, it also increases sensitivity to geometrical misalignment, modal interference, and nonuniform loss mechanisms. If the beam is allowed to exit the cavity after a single pass, parasitic effects such as optical reflections and wall heating are reduced, thereby minimizing background contributions and improving the purity of the photoacoustic signal.

ii) Finite-width Gaussian excitation
A more realistic description of a finite-width beam (e.g., partially collimated or diffuse illumination) can be obtained by modeling the absorbed optical power as a Gaussian distribution centered at Φ_0:

$$H_\Phi = \frac{P_\Phi}{\sqrt{2\pi}\sigma_\Phi} e^{-\frac{(\phi-\Phi_0)^2}{2\sigma_\Phi^2}}, \tag{11}$$

where σ_Φ defines the angular beam width, and the normalization ensures independence of the absorbed power from the angular beam. For sufficiently narrow beams, the contribution of $H(\Phi)$ outside a small neighborhood of Φ_0 is negligible, allowing the integration domain in Eq. 4 to be extended to the real line without significant error. Under this approximation, the modal coupling coefficients can be evaluated in closed form as

$$M_n \approx \frac{P_\Phi}{2\pi} e^{-\frac{(n\sigma_\Phi)^2}{2}} e^{-jn\Phi_0}. \tag{12}$$

This expression shows that a finite beam width introduces an exponential attenuation of the coupling strength for higher-order modes, effectively acting as a spatial low-pass filter in the modal domain. In the limit $\sigma_\Phi \to 0$, the δ-like excitation of Eq. 10 is recovered, while increasing σ_Φ progressively suppresses higher-order modes and enhances modal selectivity toward the fundamental. However, in the case of distributed illumination, the optical interaction extends over a larger portion of the cavity, increasing the contribution of non-selective absorption processes such as carrier gas absorption and wall heating.

As a result, a higher background level is expected compared to the case of localized excitation, potentially limiting the achievable SNR and dynamic range of the measurement [3], [12], [25].

III. Materials and Methods

A. Measurement Setup

Two optical excitation configurations were implemented to investigate the influence of light confinement on the PA response: a high-power LED and a LD, both emitting at $\lambda = 405$ nm (Fig. 1a). The two configurations shared the same resonant photoacoustic cell and detection chain, enabling a direct comparison under identical acoustic and mechanical conditions.

The resonant PA cell, previously designed and optimized in [21], is a toroidal aluminum cavity (minor radius $r_{ch} = 3.5$ mm, major radius $R_{ch} = 13.5$ mm) sealed by a top cover plate integrating the gas ports, optical windows, and microphone mount. The geometry supports the fundamental acoustic eigenmode at $f_r = 4.12$ kHz.

Optical access to the gas volume is provided by two opposed circular apertures ($D_{\text{hole}} = 3$ mm) sealed by fused-silica windows, enabling a straight beam path through the cavity and reducing internal reflections and wall-induced background. The symmetric optical layout also suppresses spurious acoustic generation in proximity to the microphone [10].

As depicted in Fig. 1b, a MEMS microphone (Knowles SPU0410LR5H-QB) is positioned at the acoustic antinode, while the gas inlet and outlet are located at pressure nodes. The microphone signal is conditioned by the low-cost electronic interface in [18] (low-noise amplification, band-pass filtering centered at f_r, and synchronous demodulation), yielding the demodulated output voltage $V_{PA}(t)$. The system is designed to operate at the acoustic cell's resonance frequency, where the photoacoustic response is maximized. Signals outside the resonance band are strongly attenuated by both the resonator and the narrowband filter, and thus contribute negligibly to the demodulated output. The adopted lock-in detection scheme was previously detailed and characterized in [18], and the same front-end has been successfully used for gas sensing in complex mixtures in [17], [18], [21], [28].

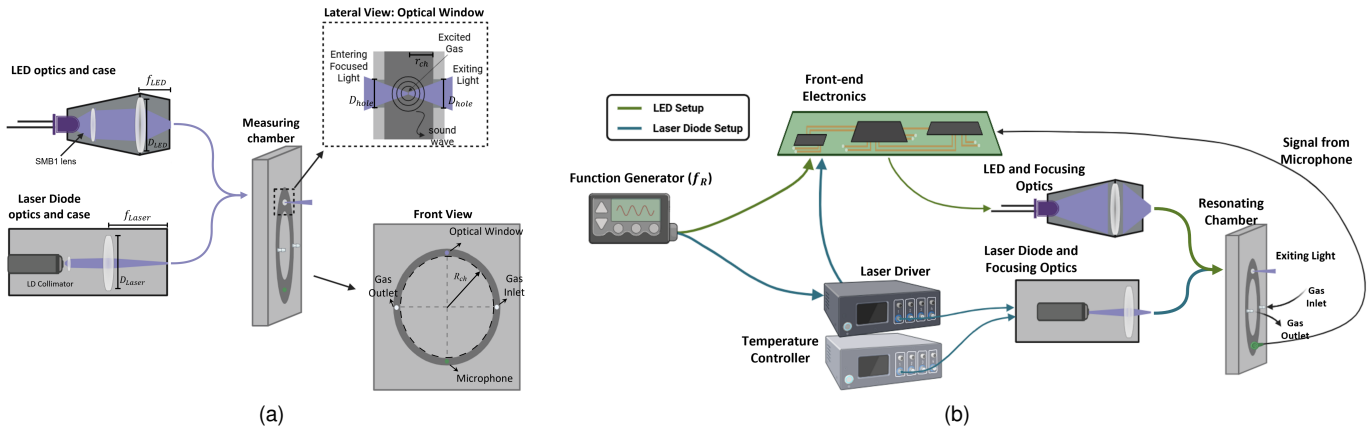

Fig. 1. (a) Optical setup employing LED and Laser excitation sources with collimation, and focusing optics. The toroidal resonant chamber. The detail of the optical window is also shown in lateral view (top right): two opening windows with a diameter (D_{hole} = 3 mm) allow the beam to pass through it only once, and it is excited in a small point (the focus) at the center of the transit path. (b) Sketch of the experimental measurement setup for NO_2 detection.

1) LED excitation configuration: The LED source used (SMB1N-405V, Roithner Lasertechnik GmbH, Vienna, Austria) provides a nominal radiant flux of $P_{\mathrm{opt}} = 710$ mW at $I = 500$ mA. The LED is driven by a front-end current driver that supplies a modulated current at the cell resonance frequency f_r with adjustable amplitude. Its broad emission cone ($\pm 63°$) is collimated with an SMB-LENS (FWHM $= 10°$) and then focused by a plano–convex lens (Thorlabs LA1951, $f_{LED} = 25$ mm, $D_{LED} = 1$ in). All optical components are housed in a custom 3D-printed mount to maintain stable alignment with the resonant chamber.

2) LD excitation configuration: The laser-based configuration employed a 405 nm diode (RLT405-1000MGE, Roithner Lasertechnik GmbH, Vienna, Austria) delivering up to 1 W optical power. The LD was operated in a temperature-stabilized mount (TCLDM9, Thorlabs Inc.) driven by a precision current controller (LDC205C, Thorlabs Inc.) and stabilized by a thermoelectric controller (TEC200C, Thorlabs Inc.) to maintain $\Delta T < 0.1°$C. The beam is collimated and then focused by a plano–convex lens (LA1131, Thorlabs, $f_{Laser} = 50$ mm) to the cell center. All optical elements were mounted on an aluminum optical rail to ensure reproducible alignment and mechanical rigidity.

B. Optical Characterization

The excitation sources were optically characterized to quantify their emitted power and the focused beam geometry under the same alignment conditions used in the photoacoustic experiments. For each source, two measurements were performed: (i) DC power–current (P–I) curves and (ii) beam-size evaluation along the propagation axis.

For the LED, the total radiant flux was measured with an integrating sphere (ETO-S20-P6-HPA, ORB Inc., USA). For the LD, the emitted power was measured with an optical power meter (Newport 1918-R) and detector (918D-UV-OD3), using the same DC drive current and temperature stabilization (Thorlabs Inc.) adopted in the gas tests. The DC P–I curves were then used to derive the RMS optical powers associated with each modulation condition (Section III-C).

Beam-size measurements were performed using the knife-edge technique [31] on a motorized translation stage (PT1, Thorlabs Inc., Newton, NJ, USA) with micrometric resolution. For beam profiling, the LED and LD were driven at $I_{\mathrm{DC}} = 250$ mA and $I_{\mathrm{DC}} = 340$ mA (200 mA above threshold), respectively. The beam radius w at each axial position was extracted by fitting the normalized power profile to an error-function model where $P'(x)$ denotes the optical power measured during the knife-edge scan as a function of the blade position x as:

$$P'(x) = P_0 \left[1 - \mathrm{erf}\left(\frac{\sqrt{2}(x - x_0)}{w} \right) \right] \tag{13}$$

where P_0 is the total power, x_0 is the beam-center position, and w represents the $1/e^2$ beam radius.

All optical measurements were conducted under the same mechanical alignment and environmental conditions later used in the NO_2 measurement experiments.

C. Gas Measurements

Gas-sensing experiments were carried out to assess how the optical–acoustic coupling inside the resonator, under the two optical excitation configurations depicted in Figure 1a, affects the resulting PA gas response. All measurements were performed using NO_2 as the target species, supplied from a certified reference mixture containing 50 ppm of NO_2 in nitrogen (N_2) as carrier gas, both provided by a specialized supplier company (SIAD S.p.A., Italy). Different concentrations were obtained by controlled dilution of the target gas with N_2 using accurate mass-flow controllers (EL-FLOW Select, Bronkhorst High-Tech B.V., Ruurlo, The Netherlands), allowing to realized mixture of the target gas with desired concentration levels. The total flow rate was maintained constant at 200 mL min^{-1} throughout all experiments to ensure constant acoustic and thermal conditions inside the chamber. A block diagram of the measurement setup used for both LED and LD configurations is shown in Fig. 1b.

Optical modulation at the resonance frequency f_r = 4.12 kHz was provided by a function generator

(Model 33220A, Agilent Technologies, Santa Clara, CA, USA). In the LD configuration (Fig. 1b), the device was installed in the same temperature-stabilized mount described above, ensuring $\Delta T < 0.1°\mathrm{C}$. The sinusoidal modulation signal was applied to the analog input of the same precision current driver (Thorlabs Inc.).

Conversely, for the LED, the waveform drove the integrated current stage on the front-end electronic board [18].

During gas measurements, the sources were operated with a sinusoidal current of peak-to-peak amplitude I_{pp}. For the LED, the current was biased with a DC offset of $I_{\mathrm{pp}}/2$, so that the excitation current varied between $I_{\min} = 0$ and $I_{\max} = I_{\mathrm{pp}}$. For the LD, the modulation was centered above threshold current ($I_{th} + I_{pp/2}$, $I_{min} = I_{th}$) to preserve linear emission. Assuming a linear relation between emitted optical power and driving current within the adopted operating range, and taking the zero-emission condition at $I_{\min}$ as reference, the instantaneous optical power can be written as

$$P_{opt}(t) = \frac{P_{max}}{2}[1 + sin(\omega t)] \tag{14}$$

where P_{max} is the peak optical power corresponding to the maximum driving current. The corresponding RMS optical power is given by

$$P_{\mathrm{RMS}} = \sqrt{\frac{1}{T}\int_0^T P_{opt}^2(t)\,dt} = P_{max}\sqrt{\frac{3}{8}} \tag{15}$$

where the factor $\frac{3}{8}$ arises from the time averaging of the squared sinusoidal waveform with DC offset. This expression was used to derive the RMS optical powers associated with the modulation conditions adopted in the gas measurements.

All measurements were carried out at room temperature $(23 \pm 2)\,°\mathrm{C}$ and atmospheric pressure within an acoustically isolated enclosure. The amplified and demodulated photoacoustic voltage signal $V_{\mathrm{PA}}(t)$ was acquired using an acquisition board (PCI-6014, NI, Austin, TX, USA), with 16-bit analog input resolution and an input range of ± 10 V. The sampling frequency was set to 1 kHz. All acquired data were processed on a PC using a dedicated virtual instrument developed in the NI LabVIEW environment.

The PA gas response was characterized through three dedicated experimental protocols, hereafter referred to as E1, E2, and E2b, described below:

- **Sensitivity and Linearity Analysis (E1):** This test evaluates the PA response sensitivity and linearity versus NO_2 concentration. The concentration was decreased from 50 ppm down to 0 ppm in 10 ppm steps, with each level held for about 1 min to ensure stable gas exchange. The E1 current settings (Table I) were chosen to directly compare LED and LD at similar optical powers (LED 300 mA, LD 290 mA) and to include an additional LD level (200 mA) to assess the sensitivity versus modulation current.
- **Repeatability and Dynamic Response (E2):** This protocol evaluates repeatability and dynamic behavior under alternating exposure to NO_2 and pure N_2. The chamber was alternately filled with 50 ppm NO_2 and pure N_2, each phase lasting about 1 min. The 0–50–0 ppm sequence was repeated for 10 cycles. The E2 current settings (Table I) were chosen to yield comparable optical power at the entrance window (LED 250 mA, LD 200 mA) and to include an additional LED drive level (300 mA).
- **Baseline Contributions under Optical Confinement (E2b):** An additional experiment (E2b) repeated the E2 protocol only for the LD source with $I_{\mathrm{pp}} = 100$ mA (Table I), and with the exit window (Fig. 1a) closed by a diffuse reflector to confine light within the resonant chamber. The lower modulation amplitude avoided saturation of the ADC input stage. This closed-window setup is not intended as a new measurement configuration, but as a control case to quantify baseline/SNR degradation due to optical confinement and wall interaction, as in earlier designs without an exit optical window [21].

TABLE I
EXPERIMENTAL MODULATION CONDITIONS. ALL SOURCES WERE DRIVEN WITH A SINUSOIDAL CURRENT WITH $f_r = 4.12$ KHZ. I_{pp} IS THE PEAK-TO-PEAK MODULATION CURRENT. THE COLOR CODE IN THIS TABLE IS USED IN THE FIGURES WHENEVER DIFFERENT LED/LD DRIVE-CURRENT CONDITIONS ARE COMPARED.

Test	Source	I_{pp} (mA)	Color
E1	LED	300	
	LD	200	
	LD	290	
E2	LED	250	
	LED	300	
	LD	200	
E2b	LD	100	

D. Signal Processing and Metric Definitions

To ensure identical reference conditions, the system was purged with pure nitrogen for at least 10 min before each test to remove residual gas. All measurements used the same optical alignment for both LED and LD excitation. The sinusoidal modulation conditions for the three gas experiments are listed in Table I. The time-dependent PA voltage at the analog front-end output is defined as $V_{\mathrm{PA}}(t)$, while the baseline PA contribution V_0 is defined as the mean PA voltage measured under pure N_2 (0 ppm), thereby accounting for background absorption in the cell walls and windows. For gas-measurement protocols E1 and E2, the average baseline-corrected photoacoustic amplitude was computed as:

$$\overline{V}_{\mathrm{PA,bc}} = \frac{1}{T_w}\int_{\mathcal{W}} \left(V_{\mathrm{PA}}(t) - V_0\right)\,\mathrm{d}t, \tag{16}$$

where $\mathcal{W}$ denotes a fixed time window of duration $T_w = 30$ s centered within the steady-state portion of the corresponding concentration plateau. This windowing strategy excludes the rising and falling transients associated with gas-exchange dynamics and retains only the stabilized response used for quantitative analysis.

The noise level σ_{noise} was estimated as the standard deviation of the baseline-corrected PA signal $V_{\mathrm{PA,bc}}(t)$ measured under pure N_2 conditions (0 ppm), evaluated over time

windows of identical duration to those used for the signal averaging. When multiple 0 ppm plateaus were available, all corresponding windows were pooled to obtain a single noise estimate, defined as:

$$\sigma_{\text{noise}} = \text{std}\{V_{\text{PA,bc}}(t)\}\big|_{0\,\text{ppm}} \tag{17}$$

Accordingly, the signal-to-noise ratio (SNR) values reported in Section IV were computed as:

$$\text{SNR} = 20\log_{10}\left(\frac{\overline{V}_{\text{PA,bc}}}{\sigma_{\text{noise}}}\right) \tag{18}$$

For the repeatability test (E2), each cycle corresponded to one full 0–50–0 ppm concentration sequence. The cycle-averaged PA amplitude was obtained by averaging all lock-in DC samples within the steady-state portion of the corresponding plateau (approximately a 1 min window). RSD and peak-to-peak drift were then computed across the 10 repeated cycles.

IV. Results and Discussion

A. Optical Characterization

In this section, the results are presented primarily to validate the proposed optical–acoustic coupling framework, rather than to provide a standalone assessment of gas sensing performance. As described in Section III-B, the optical characterization was carried out to (i) measure the DC power–current (P–I) behavior of the excitation sources and (ii) estimate the beam size after the focusing optics used in the gas measurements.

Both sources exhibited an approximately linear P–I behavior over the operating range considered (LED: quasi-linear; LD: linear above threshold). The measured DC P–I curves were then used to derive the RMS optical power corresponding to each modulation amplitude I_{pp} employed in the gas experiments (Section III-C).

Knife-edge profiling confirmed the markedly different focusing capability of the two sources, with the LD producing a much smaller waist than the LED after the same optics.This outcome supports the δ-like approximation adopted for the LD excitation in the theoretical formulation (Sec. II), particularly when contrasted with the broader LED illumination profile [32].

Table II summarizes the derived RMS optical powers and the corresponding beam size diameters.

TABLE II
RMS optical power for each current modulation tested and corresponding beam diameters for the excitation sources used in the gas measurements.

Source	I_{pp} (mA)	P_{RMS} (mW)	Beam size diameter (mm)
LED	250	189.9	7.272
	300	227.9	
LD	100	80.2	0.195
	200	162.2	
	290	235.0	

B. Gas Measurements

The photoacoustic gas response was analyzed through three experimental campaigns (E1, E2, and E2b) performed under identical flow and modulation conditions, as described in Sec. III-C.

1) Sensitivity and Linearity Analysis (E1): Gas measurements were performed under sinusoidal optical-intensity modulation at f_r (Sec. III-C) to compare LED and LD excitation. The LED was operated at $I_{\text{pp}} = 300$ mA (227.9 mW_{RMS}), while the LD was tested at $I_{\text{pp}} = 200$ mA (162.2 mW_{RMS}) and 290 mA (235.0 mW_{RMS}). Figure 2 reports the baseline-corrected response $V_{\text{PA,bc}}(t)$ during stepwise NO_2 variations.

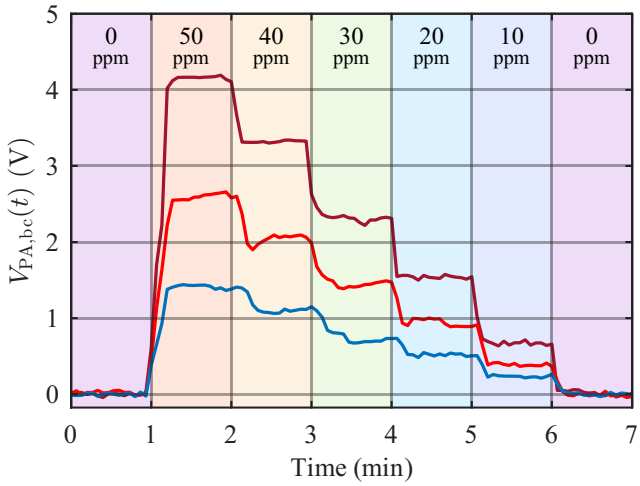

Fig. 2. Baseline-corrected PA signal $V_{\text{PA,bc}}(t)$ in time during gas measurements for both LED- and LD-configurations; NO_2 concentration varies from 50 ppm to 0 ppm. Modulation frequency f_r=4.12 kHz. Different colors refer to different current amplitudes and sources: LED at 300 mA (—), LD at 200 mA (—), and 290 mA (—). Shaded colored bands indicate the time intervals corresponding to each NO_2 concentration phase.

The corresponding linearity plots are reported in Fig. 3, together with first-order linear regression fits constrained to pass through zero. In all cases, the PA response exhibited a clear linear dependence on gas concentration. The evaluated sensitivity was 28 mV ppm^{-1} for the LED, 52.6 mV ppm^{-1} for the LD at $I_{\text{pp}} = 200$ mA, and 83 mV ppm^{-1} for the LD at $I_{\text{pp}} = 290$ mA. The maximum non-linearity errors (relative deviation from the linear fit over the explored concentration range) were 7.72% for the LED, 4.64% for the LD at 200 mA, and 3.47% for the LD at 290 mA, confirming an overall good linear behavior.

Focused LD excitation shows higher optical-to-acoustic conversion efficiency than LED excitation. Under comparable optical power (LED: $I_{\text{pp}} = 300$ mA, 227.9 mW_{RMS}; LD: $I_{\text{pp}} = 290$ mA, 235.0 mW_{RMS}), the LD yields a substantially higher sensitivity, consistent with the higher power density in the absorption region. Figure 4 reports the SNR as a function of NO_2 concentration. The maximum SNR is 44 dB for the LD at $I_{\text{pp}} = 290$ mA, whereas the LED at comparable optical power ($I_{\text{pp}} = 300$ mA) achieves approximately 37 dB.

2) Repeatability and Dynamic Response (E2): Figure 5 reports the baseline-corrected response during the E2 gas-cycling protocol, consisting of repeated 0–50–0 ppm NO_2 steps.

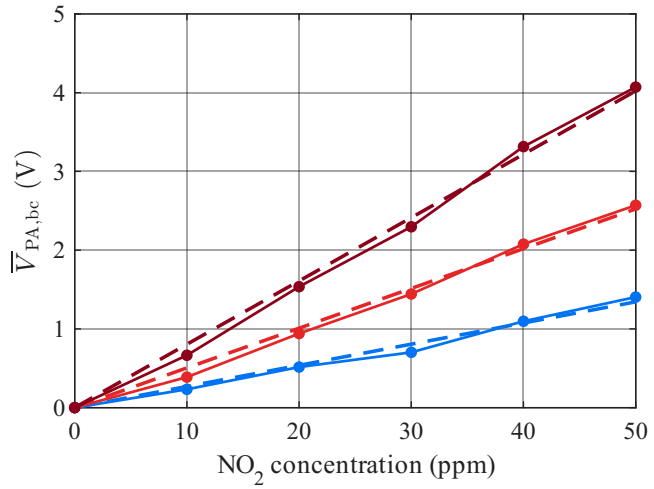

Fig. 3. Average photoacoustic response as a function of NO_2 concentration for LED and LD excitation. Measured data are shown as solid lines with markers, while dashed lines indicate first-order linear regression fits constrained to pass through zero. Colors correspond to LED excitation at $I_{\mathrm{pp}} = 300$ mA (—) and LD excitation at $I_{\mathrm{pp}} = 200$ mA (—) and $I_{\mathrm{pp}} = 290$ mA (—). The plotted amplitude corresponds to $\overline{V}_{\mathrm{PA,bc}}$ computed over 30 s steady-state windows (Section III-C); the maximum non-linearity errors were 7.72% (LED), 4.64% (LD, 200 mA), and 3.47% (LD, 290 mA).

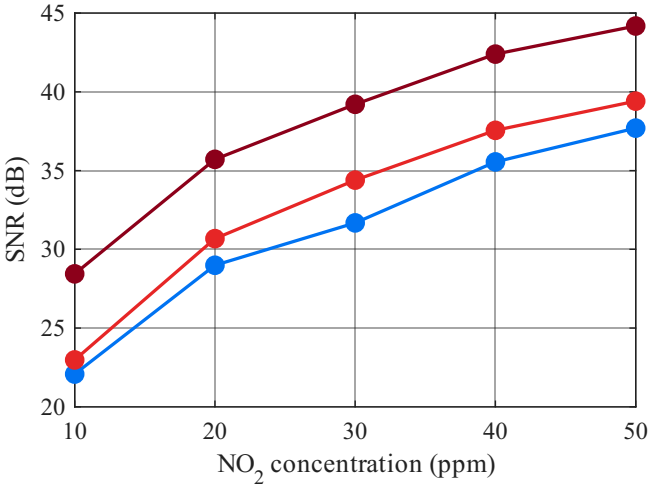

Fig. 4. Signal-to-noise ratio (SNR) as a function of NO_2 concentration for LED and LD excitation. Curves correspond to: LED at 300 mA (—); LD at 200 mA (—); and LD at 290 mA (—).

Repeatability was quantified from the steady-state segments of $V_{\mathrm{PA,bc}}(t)$ (Sec. III-D), while Fig. 5 shows three representative cycles for visualization, the repeatability metrics themselves were computed over 10 cycles using steady-state, cycle-averaged amplitudes.

At $I_{\mathrm{pp}} = 300$ mA, the LED exhibits an RSD of 0.34% and a maximum drift of 65 mV, whereas at $I_{\mathrm{pp}} = 200$ mA the LD shows an RSD of approximately 3.6% with a drift of about 177 mV; despite the higher variability, it provides a larger PA amplitude (2.47 V vs 1.1 V for the LED at 300 mA).

The dynamic response was evaluated from ensemble-averaged transitions aligned at the 50% crossing, yielding rise times of 8–9 s and fall times of approximately 12 s, which are primarily governed by gas-exchange dynamics.

3) Baseline Contributions under Optical Confinement (E2b): To quantify baseline contributions under optical confinement, the E2b configuration (E2b) was implemented with the LD source and by blocking the exit window with a diffuse reflector. Here, the LD was operated at $I_{\mathrm{pp}} = 100$ mA (80.2 $\mathrm{mW_{RMS}}$) to avoid saturation of the analog front-end, whose effective dynamic range is limited to $\approx 10\ V$ by the 12 V supply rails. Figure 6 reports the PA response $V_{PA}(t)$ obtained in E2b (LD 100 mA) together with the standard E2 configurations (LEDs and LD), without baseline subtraction. In the Figure, the signal is normalized to $V_{FS} = 10$ V as $V_{norm} = V_{PA}/V_{FS}$ to highlight the impact of $\overline{V_0}$ on the usable dynamic range. Since V_0 represents a DC offset at the output of the analog front-end, the ratio $\overline{V_0}/V_{FS}$ directly quantifies the fraction of the available ADC dynamic range consumed by baseline contributions.

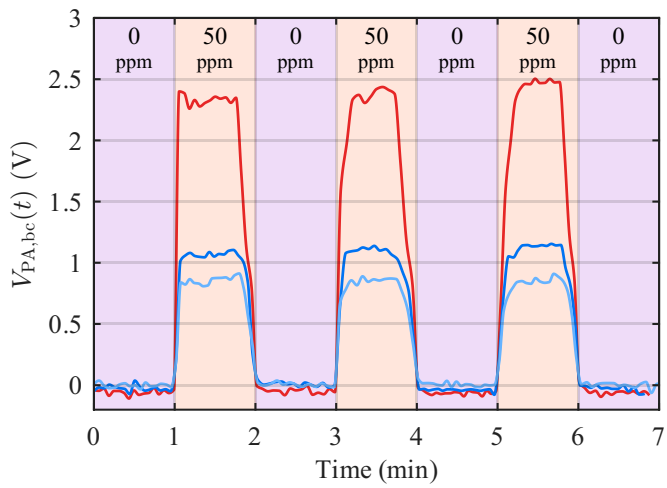

Fig. 5. Baseline-corrected PA signal $V_{\mathrm{PA}}(t) - V_0$ during the E2 gas-cycling protocol, illustrating signal repeatability. Only three representative cycles are displayed, while a total of 10 cycles were repeated. Curves correspond to LED excitation at $I_{\mathrm{pp}} = 250$ mA (—) and $I_{\mathrm{pp}} = 300$ mA (—), and LD excitation at $I_{\mathrm{pp}} = 200$ mA (—).

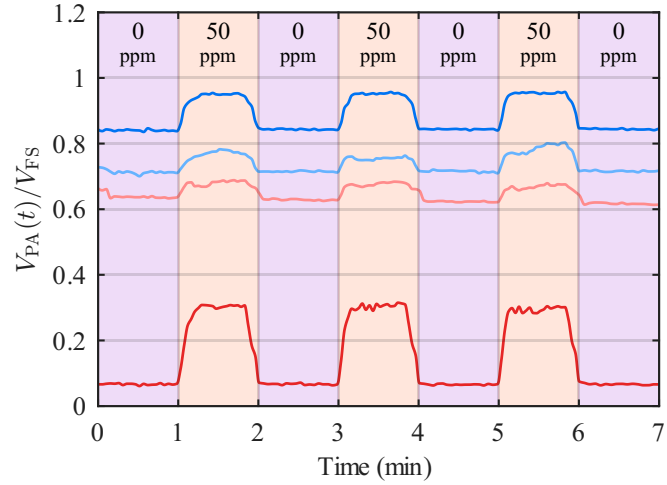

Fig. 6. Normalized PA response ($V_{\mathrm{PA}}(t)/V_{\mathrm{FS}}$) for different excitation scenarios, reported without baseline subtraction. The E2b configuration corresponds to the LD operated at $I_{\mathrm{pp}} = 100$ mA (—), where a diffuse reflector was placed at the exit window. The standard E2 configurations correspond to LD excitation at $I_{\mathrm{pp}} = 200$ mA (—) and LED excitation at $I_{\mathrm{pp}} = 250$ mA (—) and 300 mA (—).

The quantitative comparison is summarized in Table III. Configurations with strong wall interaction (LEDs in E1,E2,

and LD in E2b) exhibit high baseline levels, with $\overline{V_0}$ consuming a large fraction of the input dynamic range. In contrast, the LD without back-diffusion (E1, E2) maintains $\overline{V_0} < 0.83$ V, thus preserving more than 90% of the ADC range for the gas signal. This aspect is critical for embedded readout systems with limited full-scale inputs, where offsets observed in the LED or E2b cases would cause saturation or severely reduce resolution.

TABLE III
QUANTITATIVE ANALYSIS OF THE AVERAGE BASELINE CONTRIBUTION ($\overline{V_0}$) TO THE PA SIGNAL, AND CONSEQUENT DYNAMIC RANGE CONSUMPTION NORMALIZED TO FRONT-END BOARD FULL-SCALE ($V_{FS} = 10$ V). * E2B CONFIGURATION WITH DIFFUSE BACK-REFLECTION AT THE EXIT WINDOW.

Configuration	I/P_{OPT} (mA/mW)	$\overline{V_0}$ (V)	$\overline{V_0}/V_{FS}$
LED - E1	300 / 228	8.43	0.843
LED - E2	250 / 190	7.15	0.715
LED - E2	300 / 228	8.49	0.849
LD - E1	200 / 162	0.61	0.061
LD - E1	290 / 235	0.83	0.083
LD - E2	200 / 162	0.73	0.073
LD – E2b*	100 / 80	6.29	0.629

C. Comparative Summary

Table IV summarizes the performance of tested configurations and includes, for reference, the unfocused LED benchmark from [21]. For each case, the RMS optical power at the entrance window, the gas sensitivity (κ), the SNR (evaluated at 50 ppm NO_2), the normalized sensitivity (κ/P_{OPT}), and the estimated measurable concentration range are reported.

Sensitivity values are derived according to the adopted protocol: for E1 tests, κ is obtained from the slope of the linear fit over the full concentration range (0–50 ppm), whereas for E2 and E2b tests it is evaluated from the net photoacoustic response associated with the 0–50 ppm concentration step. The estimated concentration range is computed as $(V_{FS} - \overline{V_0})/\kappa$, with $V_{FS} = 10$ V.

TABLE IV
OVERALL PERFORMANCE EVALUATION REFERRED TO A NO_2 CONCENTRATION OF 50 PPM. κ INDICATES THE GAS SENSITIVITY, AND *EST. RANGE* INDICATES THE MAXIMUM MEASURABLE GAS CONCENTRATION LIMITED BY THE ADC DYNAMIC FULL-SCALE ($V_{FS} = 10$ V) AND BASELINE OFFSET (V_0). * E2B CONFIGURATION WITH DIFFUSE BACK-REFLECTION AT THE EXIT WINDOW.

Configuration	I_{pp}/P_{OPT} (mA/mW)	κ (mV/ppm)	SNR (dB)	κ/P_{OPT} (mV ppm^{-1} mW^{-1})	Est. Range (ppm)
Benchmark					
Unfocused LED [21]	300 / 385	29.0	43.2	0.075	~82
Current Work					
LED - E1	300 / 228	28.0	37.7	0.123	54.0
LED - E2	250 / 190	17.2	32.9	0.090	165.6
LED - E2	300 / 228	22.5	33.4	0.099	70.0
LD - E1	200 / 162	52.6	39.4	0.324	178.5
LD - E2	200 / 162	49.2	40.6	0.303	189.8
LD - E2	290 / 235	83.0	44.2	0.353	110.4
LD – E2b*	100 / 80	9.4	14.9	0.117	396.9

The results clearly identify the focused LD excitation as the most effective configuration. At comparable optical power, the LD operated at 290 mA achieves a sensitivity of 83.0 mV/ppm, approximately three times higher than the unfocused LED benchmark (29.0 mV/ppm), and a nearly fivefold increase in normalized efficiency ($\kappa/P_{OPT} = 0.353$ vs 0.075). This demonstrates that enhanced optical–acoustic coupling, achieved through tighter beam focusing and reduced light confinement within the resonant cell, is significantly more effective than increasing optical power alone.

Focused LED configurations also provide measurable improvements over the unfocused case [21], mainly in terms of reduced baseline and extended dynamic range (up to approximately a factor of two in E2). However, their performance remains limited by the large emitting area and high optical etendue, which reduce coupling efficiency and increase wall interaction, leading to higher baseline contributions.

In contrast, laser-diode excitation enables both higher sensitivity and lower baseline, thereby preserving a larger usable dynamic range and achieving superior overall performance.

The observed results confirm that the photoacoustic signal amplitude is strongly influenced by the spatial overlap between the optical excitation and the acoustic mode, highlighting the importance of properly analyzing the specific geometry and symmetry of the resonator to optimally design the optical–acoustic coupling of the system.

V. CONCLUSION

This work investigated how optical-excitation geometry influences the photoacoustic response of a ring-shaped resonant gas cell by comparing focused laser-diode and lens-coupled LED excitation at 405 nm under identical gas-testing conditions.

The results indicate that excitation geometry plays a dominant role in determining sensor performance. The tightly focused laser-diode beam, with an optical waist diameter of approximately 200 µm, enables a more efficient spatial overlap with the acoustic mode, resulting in higher photoacoustic amplitude, reduced baseline, and improved SNR. Under comparable optical power, the laser-diode configuration achieved up to a threefold increase in sensitivity compared with the LED case.

In contrast, LED excitation remains limited by the larger emitting area and optical etendue, which reduces coupling efficiency and increases wall interaction, leading to higher baseline contributions and reduced effective dynamic range. The E2b configuration further confirmed the detrimental impact of optical confinement and internal reflections on the overall performance.

Overall, the results demonstrate that controlling both beam focusing and light-exit geometry is essential to maximize sensitivity while preserving dynamic range. These findings provide practical guidelines for the design of compact, high-performance photoacoustic sensors, particularly in applications requiring low background and efficient use of limited ADC dynamic range.

ACKNOWLEDGMENTS

This work was supported in part by the PRIN-PNRR 2022 project “Portable Device for Photoacoustic Sensing of

Breath Biomarkers" (Project ID: P2022M577Y_001; CUP: B53D23023970001). The authors also acknowledge Marco Muzzarelli for his contribution to the experimental activities conducted as part of his research fellowship.

References

[1] S. Palzer, "Photoacoustic-Based Gas Sensing: A Review," *Sensors*, vol. 20, no. 9, p. 2745, May 2020. [Online]. Available: https://www.mdpi.com/1424-8220/20/9/2745

[2] Y. Pan, L. Dong, X. Yin, and H. Wu, "Compact and Highly Sensitive NO2 Photoacoustic Sensor for Environmental Monitoring," *Molecules*, vol. 25, no. 5, p. 1201, Jan. 2020, publisher: Multidisciplinary Digital Publishing Institute. [Online]. Available: https://www.mdpi.com/1420-3049/25/5/1201

[3] Z. Feng, C. Sima, T. Li, W. Wang, Y. Pan, L. Wang, Z. Ming, and P. Lu, "Highly-sensitive photoacoustic gas sensor with dual resonant modalities for simultaneous NO and NO2 detection," *Sensors and Actuators B: Chemical*, vol. 434, p. 137596, Jul. 2025. [Online]. Available: https://www.sciencedirect.com/science/article/pii/S0925400525003715

[4] A. Miklós, P. Hess, and Z. Bozóki, "Application of acoustic resonators in photoacoustic trace gas analysis and metrology," *Review of Scientific Instruments*, vol. 72, no. 4, pp. 1937–1955, Apr. 2001.

[5] W. Bai and G. J. Diebold, "Moving photoacoustic sources: Acoustic waveforms in one, two, and three dimensions and application to trace gas detection," *Journal of Applied Physics*, vol. 125, no. 6, p. 060902, Feb. 2019. [Online]. Available: https://pubs.aip.org/jap/article/125/6/060902/156242/Moving-photoacoustic-sources-Acoustic-waveforms-in

[6] D. C. Dumitras, D. C. Dutu, C. Matei, A. M. Magureanu, M. Petrus, and C. Popa, "Laser photoacoustic spectroscopy: principles, instrumentation, and characterization," *Journal of Optoelectronics and Advanced Materials*, vol. 9, no. 12, pp. 3655–3701, 2007. [Online]. Available: https://www.academia.edu/33237491/Laser_photoacoustic_spectroscopy_principles_instrumentation_and_characterization

[7] F. Bijnen, J. Reuss, and F. Harren, "Geometrical optimization of a longitudinal resonant photoacoustic cell for sensitive and fast trace gas detection," *Review of Scientific Instruments*, vol. 67, no. 8, pp. 2914–2923, 1996.

[8] J. Li, X. Gao, L. Fang, W. Zhang, and H. Cha, "Resonant photoacoustic detection of trace gas with DFB diode laser," *Optics & Laser Technology*, vol. 39, no. 6, pp. 1144–1149, Sep. 2007. [Online]. Available: https://linkinghub.elsevier.com/retrieve/pii/S0030399206001794

[9] J.-P. Besson, S. Schilt, and L. Thévenaz, "Sub-ppm multi-gas photoacoustic sensor," *Spectrochimica Acta Part A: Molecular and Biomolecular Spectroscopy*, vol. 63, no. 5, pp. 899–904, Apr. 2006. [Online]. Available: https://linkinghub.elsevier.com/retrieve/pii/S1386142505005822

[10] C. Weber, J. Kapp, J. Wöllenstein, and K. Schmitt, "Novel approach for efficient resonance tracking in photoacoustic gas sensor systems based on a light-induced wall signal," *Photoacoustics*, vol. 31, p. 100495, Jun. 2023. [Online]. Available: https://linkinghub.elsevier.com/retrieve/pii/S2213597923000484

[11] K. Chen, Y. Chen, B. Zhang, L. Mei, M. Guo, H. Deng, S. Liu, F. Ma, Z. Gong, and Q. Yu, "Highly Sensitive Photoacoustic Microcavity Gas Sensor for Leak Detection," *Sensors*, vol. 20, no. 4, p. 1164, Feb. 2020. [Online]. Available: https://www.mdpi.com/1424-8220/20/4/1164

[12] T. Biwa, Y. Ueda, H. Nomura, U. Mizutani, and T. Yazaki, "Measurement of the Q value of an acoustic resonator," *Physical Review E*, vol. 72, no. 2, p. 026601, Aug. 2005.

[13] B. Baumann, B. Kost, H. Groninga, and M. Wolff, "Calculation of quality factors and amplitudes of photoacoustic resonators," in *Proceedings of the COMSOL Conference 2006*, Frankfurt, Germany, Jan. 2006.

[14] H. Zhong, T. Duan, H. Lan, M. Zhou, and F. Gao, "Review of Low-Cost Photoacoustic Sensing and Imaging Based on Laser Diode and Light-Emitting Diode," *Sensors*, vol. 18, no. 7, p. 2264, Jul. 2018, publisher: Multidisciplinary Digital Publishing Institute. [Online]. Available: https://www.mdpi.com/1424-8220/18/7/2264

[15] J. Karhu, T. Hieta, F. Manoocheri, M. Vainio, and E. Ikonen, "LED-Based Photoacoustic NO2 Sensor with a Sub-ppb Detection Limit," *ACS Sensors*, vol. 6, no. 9, pp. 3303–3307, Sep. 2021, publisher: American Chemical Society.

[16] Y. Dong, M. Gu, G. Zhu, T. Tan, K. Liu, and X. Gao, "Fully Integrated Photoacoustic NO2 Sensor for Sub-ppb Level Measurement," *Sensors*, vol. 20, no. 5, p. 1270, Jan. 2020, publisher: Multidisciplinary Digital Publishing Institute. [Online]. Available: https://www.mdpi.com/1424-8220/20/5/1270

[17] A. Fort, M. Mugnaini, E. Panzardi, and V. Vignoli, "Full-Optical Background Noise Compensation Method in Photoacoustic Gas Measurement System," *IEEE Sensors Journal*, vol. 25, no. 6, pp. 10 233–10 242, Mar. 2025. [Online]. Available: https://ieeexplore.ieee.org/abstract/document/10872782

[18] ——, "Toward a compact low-cost electronic interface for photoacoustic based gas sensors," in *2024 IEEE International Instrumentation and Measurement Technology Conference (I2MTC)*, May 2024, pp. 1–6, iSSN: 2642-2077. [Online]. Available: https://ieeexplore.ieee.org/abstract/document/10560957

[19] T. Rück, R. Bierl, and F.-M. Matysik, "Low-cost photoacoustic NO2 trace gas monitoring at the pptV-level," *Sensors and Actuators A: Physical*, vol. 263, pp. 501–509, Aug. 2017. [Online]. Available: https://linkinghub.elsevier.com/retrieve/pii/S0924424717304843

[20] J. Li, K. Liu, W. Zhang, W. Chen, and X. Gao, "Carbon dioxide detection using NIR diode laser based wavelength modulation photoacoustic spectroscopy," *Optica Applicata*, vol. 38, no. 2, pp. 341–352, 2008.

[21] A. Fort, M. Mugnaini, E. Panzardi, V. Vignoli, F. Dötzer, and K. S. Drese, "Highly Sensitive Photoacoustic NO2 Measurement System Based on an Optimized Ring-Shaped Resonant Cell," *IEEE Transactions on Instrumentation and Measurement*, vol. 72, pp. 1–10, 2023. [Online]. Available: https://ieeexplore.ieee.org/abstract/document/10042465

[22] A. Fort, M. Mugnaini, E. Panzardi, A. Pompanin, T. Vatansever, and V. Vignoli, "Pulsed excitation of eigenmode in photoacoustic resonators for gas sensing," in *2025 IEEE International Instrumentation and Measurement Technology Conference (I2MTC)*. IEEE, May 2025, pp. 1–6, iSSN: 2642-2077. [Online]. Available: https://ieeexplore.ieee.org/abstract/document/11079202

[23] A. Fort, M. Mugnaini, E. Panzardi, and V. Vignoli, "Investigating Temperature Effects on Resonant Photoacoustic Gas Sensor: Ring-Shaped Cell Case Study," in *2024 IEEE International Symposium on Robotic and Sensors Environments (ROSE)*. IEEE, 2024, pp. 1–5. [Online]. Available: https://ieeexplore.ieee.org/abstract/document/10590927/

[24] M. Muzzarelli, G. Gibertoni, D. Goldoni, A. Marzdar, E. Panzardi, M. Grassi, P. Malcovati, M. Mugnaini, and L. Rovati, "Design optimization of a photoacoustic system for gas detection in exhaled breath," in *2025 IMEKO TC2 International Symposium on Modern Photonic Metrology (IMEKO PhotoMet 2025)*, Modena, Italy, Sep. 2025.

[25] A. V. Gorelik and V. S. Starovoitov, "Small-size resonant photoacoustic cell with reduced window background for laser detection of gases," *Optics and Spectroscopy*, vol. 107, no. 5, pp. 830–835, Nov. 2009.

[26] L. S. Gordon, I. E. Rothman and al., "The HITRAN2020 molecular spectroscopic database," *Journal of Quantitative Spectroscopy and Radiative Transfer*, vol. 277, p. 107949, Jan. 2022.

[27] A. C. Vandaele, C. Hermans, S. Fally, M. Carleer, M. F. Mérienne, A. Jenouvrier, B. Coquart, and R. Colin, "Absorption cross-sections of NO2: Simulation of temperature and pressure effects," *Journal of Quantitative Spectroscopy and Radiative Transfer*, vol. 76, no. 3, pp. 373–391, Feb. 2003.

[28] E. Panzardi, K. S. Drese, M. Mugnaini, L. Parri, V. Vignoli, and A. Fort, "A photoacoustic-based measurement system for dual detection of no2 and co2 in combustion exhaust gases," *IEEE Transactions on Instrumentation and Measurement*, vol. 72, pp. 1–11, 2023.

[29] M. GadAllah, A. Mohamed, and A. Hefnawy, "A mathematical model for simulating photoacoustic signal generation and propaga- tion in biological tissues," *Opt Quant Electron*, vol. 5, no. 56, 2024.

[30] C. C. Lawrenson, L. D. Lafleur, and F. D. Shields, "The solution for the propagation of sound in a toroidal waveguide with driven walls (the acoustitron)," *Journal of the coustical Society of America*, vol. 103, pp. 1253–1260, 1998. [Online]. Available: https://api.semanticscholar.org/CorpusID:120472212

[31] V. Argueta-Diaz, "Knife-edge technique," in *Optical Sensors: An Introduction with Lab Demonstrations*. IOP Publishing, Aug. 2023.

[32] S. Agrawal, M. Kuniyil Ajith Singh, K. Johnstonbaugh, D. C. Han, C. R. Pameijer, and S.-R. Kothapalli, "Photoacoustic imaging of human vasculature using led versus laser illumination: A comparison study on tissue phantoms and in vivo humans," *Sensors*, vol. 21, no. 2, p. 424, 2021.